

## Carrier-envelope phase-tagged imaging of the controlled electron acceleration from SiO<sub>2</sub> nanospheres in intense few-cycle laser fields

S Zherebtsov<sup>1</sup>, F Süßmann<sup>1</sup>, C Peltz<sup>2</sup>, J Plenge<sup>3</sup>, K J Betsch<sup>1</sup>, I Znakovskaya<sup>1</sup>, A S Alnaser<sup>1,4,5</sup>, N G Johnson<sup>1,6</sup>, M Kübel<sup>1</sup>, A Horn<sup>1</sup>, V Mondes<sup>3</sup>, C Graf<sup>3</sup>, S A Trushin<sup>1</sup>, A Azzeer<sup>4</sup>, M J J Vrakking<sup>7</sup>, G G Paulus<sup>8,9</sup>, F Krausz<sup>1</sup>, E Rühl<sup>3</sup>, T Fennel<sup>2,10</sup> and M F Kling<sup>1,6,10</sup>

<sup>1</sup> Max-Planck Institut für Quantenoptik, Hans-Kopfermann-Strasse 1, 85748 Garching, Germany

<sup>2</sup> Institut für Physik, Universität Rostock, Universitätsplatz 3, 18051 Rostock, Germany

<sup>3</sup> Physical Chemistry, Freie Universität Berlin, Takustrasse 3, 14195 Berlin, Germany

<sup>4</sup> Physics and Astronomy Department, King-Saud University, Riyadh 11451, Saudi Arabia

<sup>5</sup> Physics Department, American University of Shariyah, PO Box 26666, Shariyah, UAE

<sup>6</sup> JR Macdonald Laboratory, Kansas-State University, Manhattan, KS 66506, USA

<sup>7</sup> Max-Born Institut, Max-Born Strasse 2A, 12489 Berlin, Germany

<sup>8</sup> Friedrich-Schiller-Universität Jena, Max-Wien Platz 1, 07743 Jena, Germany

<sup>9</sup> Helmholtz Institut Jena, 07743 Jena, Germany

E-mail: [thomas.fennel@uni-rostock.de](mailto:thomas.fennel@uni-rostock.de) and [matthias.kling@mpq.mpg.de](mailto:matthias.kling@mpq.mpg.de)

*New Journal of Physics* **14** (2012) 075010 (17pp)

Received 1 March 2012

Published 10 July 2012

Online at <http://www.njp.org/>

doi:10.1088/1367-2630/14/7/075010

**Abstract.** Waveform-controlled light fields offer the possibility of manipulating ultrafast electronic processes on sub-cycle timescales. The optical light-wave control of the collective electron motion in nanostructured materials is key to the design of electronic devices operating at up to petahertz frequencies. We have studied the directional control of the electron emission from 95 nm

<sup>10</sup> Authors to whom any correspondence should be addressed.

diameter SiO<sub>2</sub> nanoparticles in few-cycle laser fields with a well-defined waveform. Projections of the three-dimensional (3D) electron momentum distributions were obtained via single-shot velocity-map imaging (VMI), where phase tagging allowed retrieving the laser waveform for each laser shot. The application of this technique allowed us to efficiently suppress background contributions in the data and to obtain very accurate information on the amplitude and phase of the waveform-dependent electron emission. The experimental data that are obtained for 4 fs pulses centered at 720 nm at different intensities in the range  $(1-4) \times 10^{13} \text{ W cm}^{-2}$  are compared to quasi-classical mean-field Monte-Carlo simulations. The model calculations identify electron backscattering from the nanoparticle surface in highly dynamical localized fields as the main process responsible for the energetic electron emission from the nanoparticles. The local field sensitivity of the electron emission observed in our studies can serve as a foundation for future research on propagation effects for larger particles and field-induced material changes at higher intensities.

## Contents

<b>1. Introduction</b>	<b>2</b>
<b>2. Experimental approach</b>	<b>4</b>
2.1. Velocity-map imaging of electron emission from isolated nanoparticles . . . . .	4
2.2. Background suppression . . . . .	6
<b>3. Theoretical approach</b>	<b>8</b>
<b>4. Experimental results and comparison with the model calculations</b>	<b>9</b>
4.1. Intensity dependence of the electron emission . . . . .	9
4.2. Imaging the electron rescattering . . . . .	12
<b>5. Conclusions and outlook</b>	<b>15</b>
<b>Acknowledgments</b>	<b>16</b>
<b>References</b>	<b>16</b>

## 1. Introduction

Electron motion in condensed matter driven by intense light waves in the visible can proceed on attosecond timescales, where the propagation of electrons is restricted to nanometer dimensions. Laser pulses with well-defined electric field waveforms provide an ideal tool for manipulating this motion and offer a unique spatio-temporal control on nanometer spatial and attosecond temporal scales [1, 2]. Such laser pulses in the few-cycle regime have been used to control the electron emission and acceleration from atoms [3, 4], high-harmonic generation [5], electron localization in molecules [6, 7], electron emission and acceleration from nanospheres [8] and from nanotips [9] and to control the electron emission from solids [10]. Theoretical studies have further predicted their application in the control of the optical and electronic properties of solids [11] and plasmonic fields in nanostructured surfaces for electron acceleration [12] and the generation of attosecond extreme-ultraviolet pulses [13]. Consequently, application of such laser fields to nanostructured materials has a high potential for the control of ultrafast nonlinear processes at the nanoscale, with important implications in enhancing laser-driven

electron acceleration [14, 15], the generation of extreme ultraviolet radiation at high repetition rates [16, 17] and the design of lightwave-driven electronic devices for information processing in optical communication [18].

We have recently reported on the controlled electron acceleration from SiO<sub>2</sub> nanoparticles [8]. Our studies were conducted on a beam of isolated SiO<sub>2</sub> nanoparticles. This approach has the advantage that the sample is exchanged for every laser shot and the ultrafast response of the system can be studied at laser intensities even beyond the damage threshold of the material. High-kinetic-energy electrons with cutoff energies reaching  $53U_p$ , where  $U_p$  is the ponderomotive potential, were observed. Furthermore, the directional emission of the electrons was controlled by the laser waveform of a few-cycle pulse. Theoretical modeling suggested that the high-energy gain is caused by the rescattering of the electrons in the dynamically enhanced near fields of the nanoparticles. Here, we have significantly extended our studies presented in [8], as detailed below.

The electric field of a laser pulse consisting of only a few optical cycles can be described as  $E(t) = E_0(t)\cos(\omega t + \varphi)$ , where  $E_0(t)$  is the amplitude envelope function,  $\omega$  the angular frequency of the carrier wave and  $\varphi$  the carrier-envelope phase (CEP). The field evolution of such ultrafast laser fields critically depends on the value of the CEP. Our previous work [8] and many previous works (see, e.g., [19]) were based on the generation of few-cycle laser pulses with well-defined waveforms employing CEP stabilization [5, 20]. Despite significant progress in laser technology, active CEP stabilization remains an experimentally challenging task, currently limiting the continuous phase-stabilized measurements to typically a few hours. Furthermore and more importantly for the studies discussed here, laser fluctuations cannot easily be accounted for in the data acquisition with CEP-stabilized pulses, such that the analysis of CEP-dependent data was often restricted to asymmetries (normalized differences) of the forward and backward emissions rather than absolute directional electron (or ion) yields. We have recently introduced an approach where the CEP of each laser pulse was measured by a single-shot phase meter [21] and used to phase-tag single-shot data from momentum imaging experiments employing VMI [22] and reaction microscopy [23]. Here, we use this technique to investigate the electron emission from 95 nm diameter SiO<sub>2</sub> nanoparticles. The phase-tagging approach allows efficient suppression of background contributions in the experimental data and the accurate retrieval of the CEP-dependent electron yield amplitudes and phases for each point in the projected two-dimensional (2D) momentum images. The advantage of working with the projected images is the absence of any assumptions on the symmetry of the electron momentum distribution, as imposed in the regular VMI-based photoemission analysis via the Abel inversion procedure. Furthermore, the direct analysis of the CEP-dependent signal removes the cross-coupling of forward and backward emission channels in the usual analysis of forward-backward asymmetries.

The CEP-dependent electron yields and electron emission asymmetries recorded for 4 fs pulses at 720 nm at intensities in the range of  $(1-4) \times 10^{13} \text{ W cm}^{-2}$  are in excellent agreement with the results of semi-classical mean-field Monte-Carlo simulations. The comparison of the momentum-resolved amplitudes and phases of the CEP-dependent signal with theory offers unprecedented insights into the underlying electron acceleration mechanisms. Firstly, the symmetry of the amplitude and phase maps with respect to the direction of laser propagation demonstrates that the nanoparticle response is not affected by field propagation and retardation effects in the investigated size regime. Secondly, the overall structure and symmetry properties of the amplitude and phase maps in the direction of the polarization axis show the phase

selectivity of the emission from different sides of the nanoparticle and confirm that electron backscattering from the surface is a major process for the CEP-dependent generation of energetic electrons.

## 2. Experimental approach

### 2.1. Velocity-map imaging of electron emission from isolated nanoparticles

Intense laser pulses (790 nm central wavelength, 25 fs pulse duration and 1 kHz repetition rate) delivered by an amplified laser system, described elsewhere [24, 25], were spectrally broadened by a hollow core fiber filled with 2.8 bar of Ne gas and compressed by chirped mirrors to a pulse duration of 4 fs at 720 nm central wavelength and with up to 600  $\mu$ J pulse energy. The few-cycle laser beam was split into two parts. The main part (80%) of the laser output was focused into the center of a VMI detector's electrostatic lens system where it was intersected with a jet of nanoparticles. A schematic diagram of the experimental setup is presented in figure 1(a). The laser intensity in the experiment was adjusted by a continuously variable neutral optical density filter. The dispersion of the laser pulses was optimized with a pair of glass wedges in order to minimize the pulse duration inside the VMI chamber. The electrostatic lens of the VMI was used to project the momentum distribution of the emitted electrons onto an imaging microchannel plate (MCP)/phosphor screen assembly. To reduce background signals, the voltage across the MCP was gated using a high-voltage switch with a gate width of 100 ns. The velocity-map images on the phosphor screen were recorded by a high-speed digital complimentary metal-oxide-semiconductor (CMOS) camera at the full repetition rate of the laser. The camera software applied flat-field correction for each frame and only pixels with a sufficient brightness (corresponding to electron hits on the MCP) were transferred to the computer in order to reduce the number of experimental data and enable the storage of single-shot images (see [22] for details).

The SiO<sub>2</sub> nanoparticles were prepared by wet chemical synthesis. Specifically, small silica seed particles were first prepared using the Stöber procedure [26]. In subsequent reaction steps these particles were grown larger by a seeded growth process [27–29]. The standard deviation ( $2\sigma$ ) of the samples is less than 6%. After the synthesis, the particles were purified by repeated (at least three times) centrifugation/redispersion in ethanol. Transmission electron microscopy (TEM) images were taken using a Zeiss EM 10 CR in order to determine the size and the size distribution of the particles. Figure 1(c) shows a typical TEM image of the  $95 \pm 6$  nm spherical SiO<sub>2</sub> particles used in this study. A beam of nanoparticles was prepared by aerosol techniques and delivered into the interaction region by aerodynamic lens focusing [30, 31] (see figure 1(a)). This method employs the generation of an aerosol by injecting a carrier gas (here N<sub>2</sub>) into a low-concentration nanoparticle suspension. The solvent (ethanol) is dried out before injection into the aerodynamic lens.

The aerodynamic lens consists of a set of properly sized apertures and focuses the nanoparticle stream to a diameter of  $\sim 0.5$  mm in the interaction region [32] inside the VMI. The carrier gas is removed between the last aperture of the aerodynamic lens and the VMI chamber by three consecutive differential pumping stages (not shown). The particle density in the interaction region is estimated to be about  $1 \times 10^6$  nanoparticles cm<sup>-3</sup>. The velocity of the nanoparticles in the beam is sufficiently high such that nanoparticles in the interaction volume are replaced between consecutive laser shots. The experiments were performed at a typical

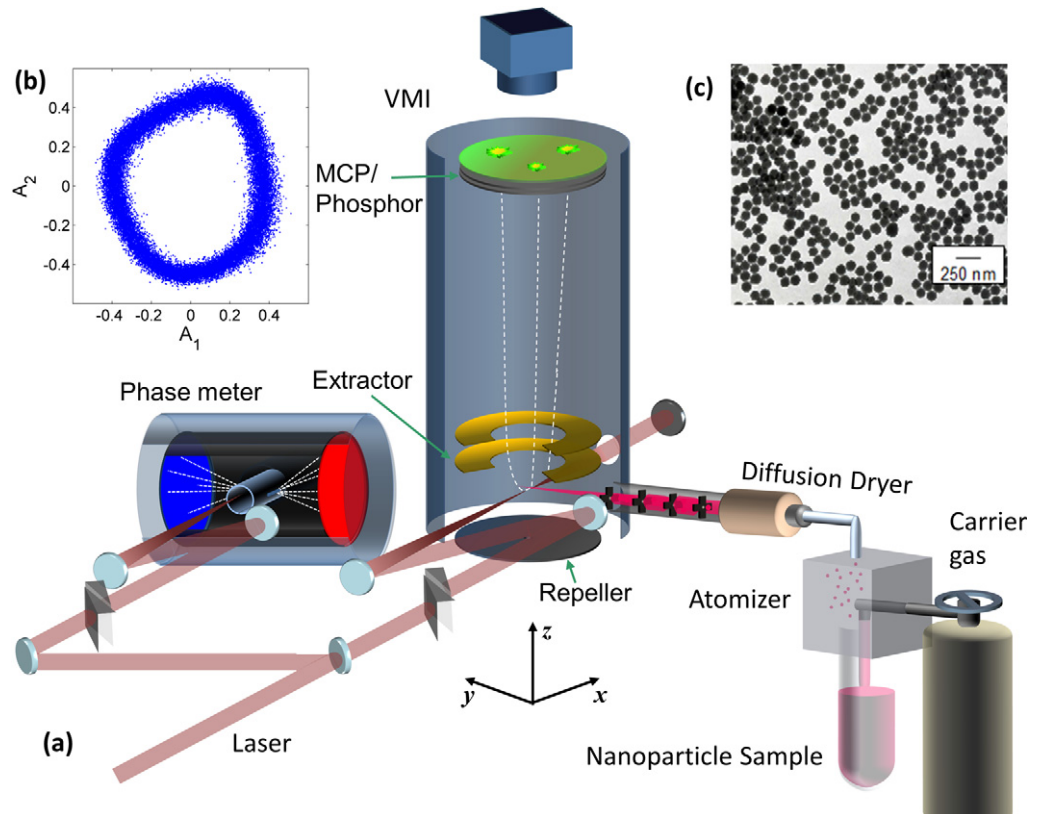


**Figure 1.** (a) Schematic diagram of the experimental setup. The VMI spectrometer consists of the charged particle imaging optics (repeller, extractor and ground plate), flight tube and an MCP/phosphor screen detector. The polarization of the laser field was in the plane of the detector. The phase meter consists of two opposing TOF spectrometers, arranged along the laser polarization axis (to the left and right). (b) PAP obtained from the phase meter for 30 000 consecutive laser shots. (c) TEM image of 95 nm diameter  $\text{SiO}_2$  nanoparticles.

pressure in the VMI chamber of  $2 \times 10^{-8}$  mbar without and at  $1 \times 10^{-6}$  mbar with the operating nanoparticle source.

Above-threshold ionization (ATI) of Xe atoms served as a reference to determine the laser pulse parameters in the interaction volume inside the VMI [8, 33]. The gas was introduced into the high-vacuum experimental chamber through a  $100 \mu\text{m}$  diameter hole in the center of the repeller of the VMI forming an effusive gas jet. The laser pulse intensity was derived from the cutoff in the ATI electron kinetic energy spectra through comparison to the semi-classical cutoff energy of  $E_{\text{cutoff}} = 10.007U_p + 0.538I_p$ , where  $I_p$  is the ionization potential of Xe [34].

To measure the CEP of each laser pulse, the weaker part (20%) of the few-cycle laser beam was focused into a single-shot phase meter (for details see [21]). The phase meter consisted of two opposing time-of-flight (TOF) spectrometers, arranged along the laser polarization axis (to the left and right); see figure 1(a) [21]. For each laser shot, the left and right TOF spectra of the electrons emitted along the laser polarization axis were integrated within two appropriate time windows 1 and 2 and the two asymmetry parameters  $A_{1,2} = (L_{1,2} - R_{1,2}) / (L_{1,2} + R_{1,2})$  were

calculated. Here  $L_{1,2}$  and  $R_{1,2}$  denote the signals of the left and right detectors, respectively, integrated within the time windows 1 and 2. The CEP  $\varphi$  was obtained from the two asymmetry parameters  $A_1$  and  $A_2$  by a parametric asymmetry plot (PAP) (see figure 1(b) for an example and [35] for details). The synchronization of the CEP and the VMI measurements for each laser shot allowed assignment of the CEP to each acquired VMI image and to sort the images into phase bins (in the present study a bin size of  $18^\circ$  was used). The data within each phase bin were summed up and 20 images corresponding to different CEPs were obtained. It should be noted that the phase meter measures only the CEP of the laser pulses up to an unknown phase offset between the phase meter and the VMI. We have calibrated the absolute CEP in the VMI by comparison of the CEP-dependent ATI in Xe, measured at the same laser parameters as the nanoparticles, with the solution of the time-dependent Schrödinger equation (TDSE) in the single-active electron approximation.

## 2.2. Background suppression

For a single laser shot, the number of electrons emitted from the nanoparticles is typically much larger than the ATI electron emission from the residual carrier gas. As the nanoparticle density in the interaction volume is limited, typically less than one nanoparticle is illuminated by each laser shot, a significant number of single-shot images contain no signal from nanoparticle targets. The average of all acquired images therefore contains a significant background signal, in particular at low electron momenta. We have recently demonstrated that the single-shot VMI detection of the electron emission from nanoparticles allows for an effective reduction of the background in the accumulated momentum images [22]. Every detected electron produces a bright spot in the camera image consisting typically of one to several pixels depending on the camera settings. The number of illuminated pixels per frame (event number) is therefore directly related to the number of emitted electrons. As shown in figure 2, selecting only frames with event numbers larger than a chosen threshold value can efficiently reduce background contributions to the overall signal. As an example, figure 2(a) shows the accumulated electron emission momentum image at a laser intensity of  $3.7 \times 10^{13} \text{ W cm}^{-2}$ . At low momenta, ATI from the background gas (mostly from residual ethanol in our experiment) dominates the image. The CEP dependence of the directional emission along the laser polarization axis (parallel to  $p_y$ ) is displayed in figure 2(b). Here, the asymmetry parameter  $A(p_y, \varphi) = (P_{\text{up}}(p_y, \varphi) - P_{\text{down}}(p_y, \varphi)) / (P_{\text{up}}(p_y, \varphi) + P_{\text{down}}(p_y, \varphi))$  for the electron emission as a function of the CEP  $\varphi$  is shown, where  $P_{\text{up}}(p_y, \varphi)$  and  $P_{\text{down}}(p_y, \varphi)$  are the angle-integrated electron yields (within the  $[-25^\circ, +25^\circ]$  angular range) in the up (positive  $p_y$  momentum) and down (negative  $p_y$  momentum) directions. The oscillations of the asymmetry parameter with CEP exhibit different phase offsets for different  $p_y$  values, resulting in the tilted pattern in the asymmetry map. The signal from the background ATI at low momenta shows slopes in the asymmetry maps similar to that observed previously for atoms [36]. The nanoparticle contribution at larger momenta shows a much steeper asymmetry pattern. Figure 2(c) shows the momentum image measured without nanoparticles (ethanol only), resembling the background ATI signal that is recorded with nanoparticles.

For a more detailed description, figure 2(d) shows a histogram of the event numbers per frame for the ethanol only (black line) and the nanoparticle in ethanol (blue line) measurements. The ethanol only signal shows a narrow distribution, which peaks at the low event numbers (corresponding to a low number of emitted electrons), while the signal from the nanoparticle

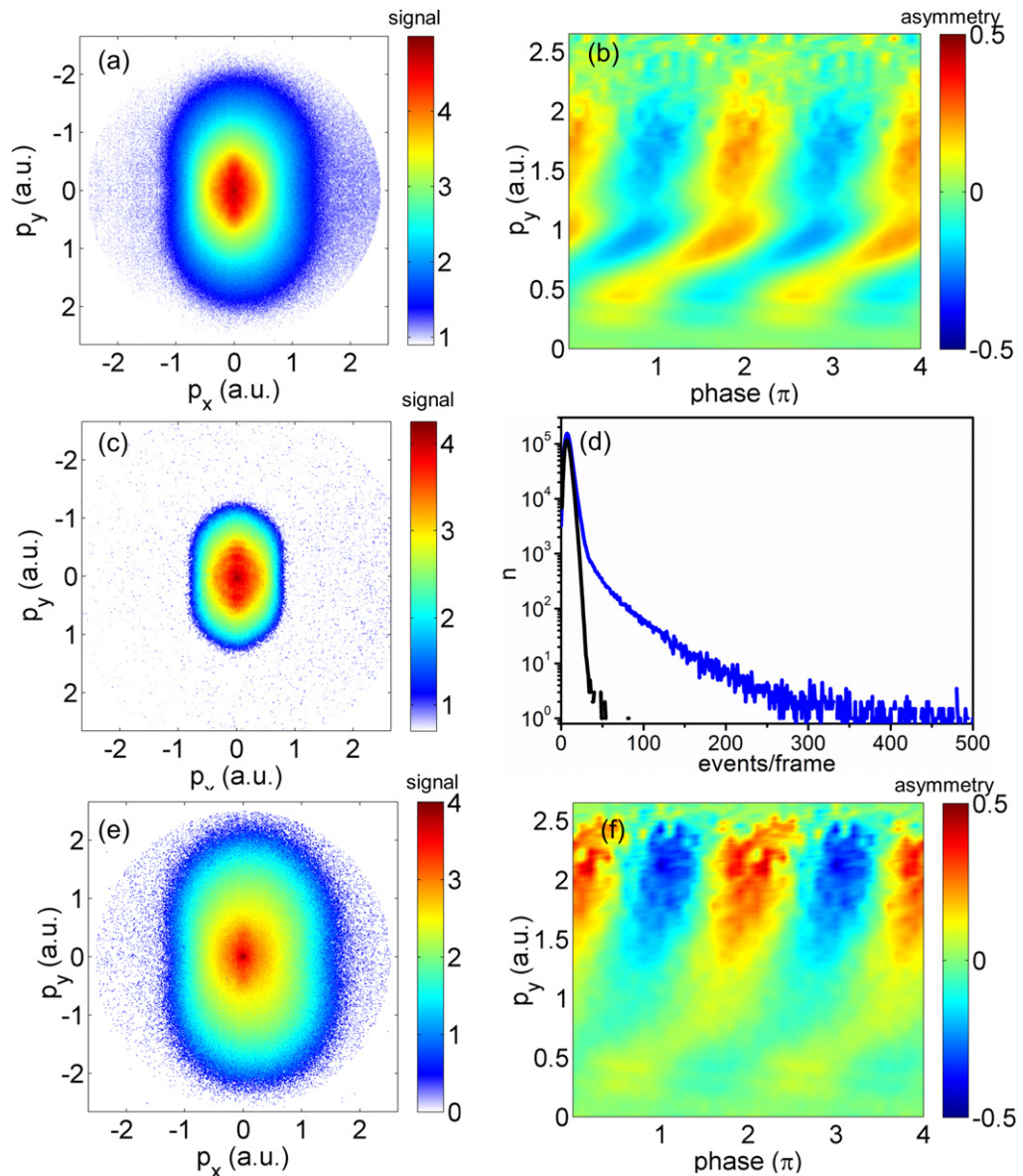


**Figure 2.** Integrated VMI images (log color scale) measured with the SiO<sub>2</sub> nanoparticles in ethanol (a) and ethanol only (c). Asymmetry of the electron emission as a function of the electron momentum and the CEP measured for SiO<sub>2</sub> nanoparticles in ethanol (b). Histograms of the number of events per frame for SiO<sub>2</sub> nanoparticles in ethanol (blue line) and ethanol only (grey line) (d). VMI images obtained for SiO<sub>2</sub> nanoparticles in ethanol (e) and the asymmetry map (f) considering only frames with more than 30 events. Hartree atomic units (au) were used for the momentum scale, where  $1 \text{ au} = 1.99285 \times 10^{-24} \text{ kg m s}^{-1}$ .

sample contains frames with a much higher number of events (corresponding to a higher number of emitted electrons). By neglecting the frames with low event numbers in the nanoparticle measurements, the background contribution can be efficiently reduced. Figures 2(e) and (f) show the data from the same experimental scan as in (a, b) but now only taking into account frames

with event numbers larger than 30 (this number was estimated as the point up to which the background ATI signal dominates). As can be clearly seen in the momentum plot, as well in the asymmetry map, the procedure efficiently suppresses the background ATI features, especially at small momenta, and thus substantially improves the analysis of the electron emission from the nanoparticles in this momentum region.

### 3. Theoretical approach

For modeling the electron emission from the nanoparticles, we use a quasi-classical trajectory-based mean field Monte-Carlo approach (M<sup>2</sup>C). The removal of electrons from the nanoparticle surface and their subsequent classical propagation are considered to be driven by the effective field produced by the laser, the nanoparticle polarization and free charges. The latter two contributions reflect the many-particle character of the target and result in pronounced field enhancement effects when compared to the atomic case. Both the initial ionization step and scattering processes of electrons that return to the nanoparticle are described stochastically with rate equations, similar to Monte-Carlo simulations for charge transport in bulk semiconductors [37]. The classical trajectories are interpreted as the center-of-mass motion of the corresponding electronic quantum wavepackets; interference effects are neglected.

In the simulations, nanoparticles are initially neutral dielectric spheres centered at the origin with radius  $R$  and purely real relative permittivity of amorphous SiO<sub>2</sub> at 720 nm ( $\varepsilon = 2.12$ ) [38]. In the dipole approximation, the laser electric field,  $E_{\text{las}}$ , and the induced medium polarization are in phase, leading to a total electric potential [39]

$$\Phi^{\text{sphere}}(r) = \begin{cases} -E_{\text{las}} \left( 1 - \frac{\varepsilon - 1}{\varepsilon + 2} \frac{R^3}{r^3} \right) y, & r \geq R, \\ -E_{\text{las}} \left( \frac{3}{\varepsilon + 2} \right) y, & r < R. \end{cases} \quad (1)$$

Nonlinear terms and dynamical changes in the dielectric response are neglected, as their contributions are negligible for the laser parameter range studied here ( $\Delta\varepsilon$  is less than 1%) [40–42].

When neglecting additional fields from free charges, the dipole approximation predicts the strongest field enhancement at the particle poles, i.e. at  $y = -R$  and  $y = +R$ . On the  $y$ -axis, the effective electric field is as follows:

$$E_y^{\text{sphere}} = \alpha E_{\text{las}}, \quad \text{with } \alpha_{|y| \geq R} = 1 + \frac{\varepsilon - 1}{\varepsilon + 2} \frac{2R^3}{|y|^3} \quad \text{and} \quad \alpha_{|y| < R} = \frac{3}{\varepsilon + 2}, \quad (2)$$

and exhibits a field enhancement of  $\tilde{\alpha} = 1.54$  over the pure laser field at the particle poles. A simple estimate of the impact of the near-field enhancement on the electron energy spectra can be made based on the classical cutoff laws for direct and backscattering electrons [43, 44] from atomic ATI. For small electron excursion lengths ( $\sim 1$  nm) the spatial variation of the field amplification can be neglected for the particle diameter considered here ( $\sim 100$  nm), resulting in an enhanced effective ponderomotive potential and modified classical cutoffs for direct and backscattered electrons of  $2\tilde{\alpha}^2 U_p = 4.74 U_p$  and  $10\tilde{\alpha}^2 U_p = 23.72 U_p$ , respectively. Note that these first-order estimates neglect the effects of (i) a finite tunnel length, (ii) the influence of the Coulomb potential from free and residual charges and (iii) field propagation. Processes (i) and

(ii) are resolved in the Monte-Carlo simulations as described below and have a profound impact on the CEP-dependent electron emission in the investigated parameter regime. Process (iii) is of minor importance for the investigated particle size range, as the impact of field retardation on the evolution of the near fields is still negligibly small. To justify the dipole approximation we performed test simulations with the full Mie solution of the near field and find no notable difference.

Within the Monte-Carlo simulations, tunnel ionization of atoms in the surface layer of the nanoparticle is assumed to be a major process for electron liberation and is approximated by the instantaneous atomic Ammosov–Delone–Krainov (ADK) tunnel ionization rates [45] using the effective field at the surface and the ionization potential of atomic Si (8.16 eV) [46]. Trajectories are launched in each time step with a statistical weight according to the local tunnel ionization rate and zero initial velocity at the classical tunnel exit.

After being released, classical electron trajectories are calculated by solving the classical equations of motion  $\ddot{r} = \frac{e}{m} \nabla \Phi^{\text{eff}}(r)$  for each electron trajectory in the effective potential  $\Phi^{\text{eff}}(r) = \Phi^{\text{sphere}}(r) + \Phi^{\text{free}}(r)$ , where  $e$  and  $m$  are the elementary charge and the electron mass, and  $\Phi^{\text{free}}$  is the Coulomb potential produced by free charges, i.e. previously liberated electrons and residual ions at the surface of the nanoparticle. The latter term describes space- and surface charge effects on the mean field level and is determined self-consistently via a radius-dependent multipole expansion up to the octupole term. The use of a multipole expansion is key to reaching the required sub-nanometer radial resolution of the dynamical fields from free carriers and the efficient solution of the dynamics, as it preserves the linear scaling of the computation time of the simulations with the number of trajectories. If electron trajectories re-penetrate the nanoparticle, elastic electron–ion scattering is evaluated via Monte-Carlo sampling assuming an isotropic cross section and a constant mean free path,  $\lambda_{\text{mfp}} = 1$  nm, similar to the effective attenuation length in SiO<sub>2</sub> [47]. Note that the results are only weakly dependent on the value of  $\lambda_{\text{mfp}}$ . Scattering remains active as long as the electron propagates inside the nanoparticle. Energy losses through electron–phonon scattering and electron impact ionization are neglected, as elastic scattering is dominant in SiO<sub>2</sub> for the relevant electron kinetic energies of a few to tens of eV [48].

For calculating the phase-dependent electron emission, simulations are performed for 40 different CEP values for a series of intensities. In each simulation the number of scattering events is recorded for each trajectory, which allows identification of direct, recollision-induced (backscattering) and regular collisional electron heating due to multiple scattering inside the dielectric particle. For comparison with the experiment, 2D focal averaging of the intensity-resolved spectra is performed.

## 4. Experimental results and comparison with the model calculations

### 4.1. Intensity dependence of the electron emission

Figure 3 presents the results of the measurements on SiO<sub>2</sub> nanoparticles of 95 nm diameter at laser intensities in the range of  $(1\text{--}4) \times 10^{13} \text{ W cm}^{-2}$  (two upper panels). The laser polarization is aligned along the  $p_y$ -axis. Only frames containing nanoparticle signal (as discussed in section 2) were considered. It should be noted that, even after background suppression, the background ATI signal still contributes significantly at low momenta for laser intensities above  $\sim 3 \times 10^{13} \text{ W cm}^{-2}$ . For comparison, the theoretical results from the mean field Monte-Carlo

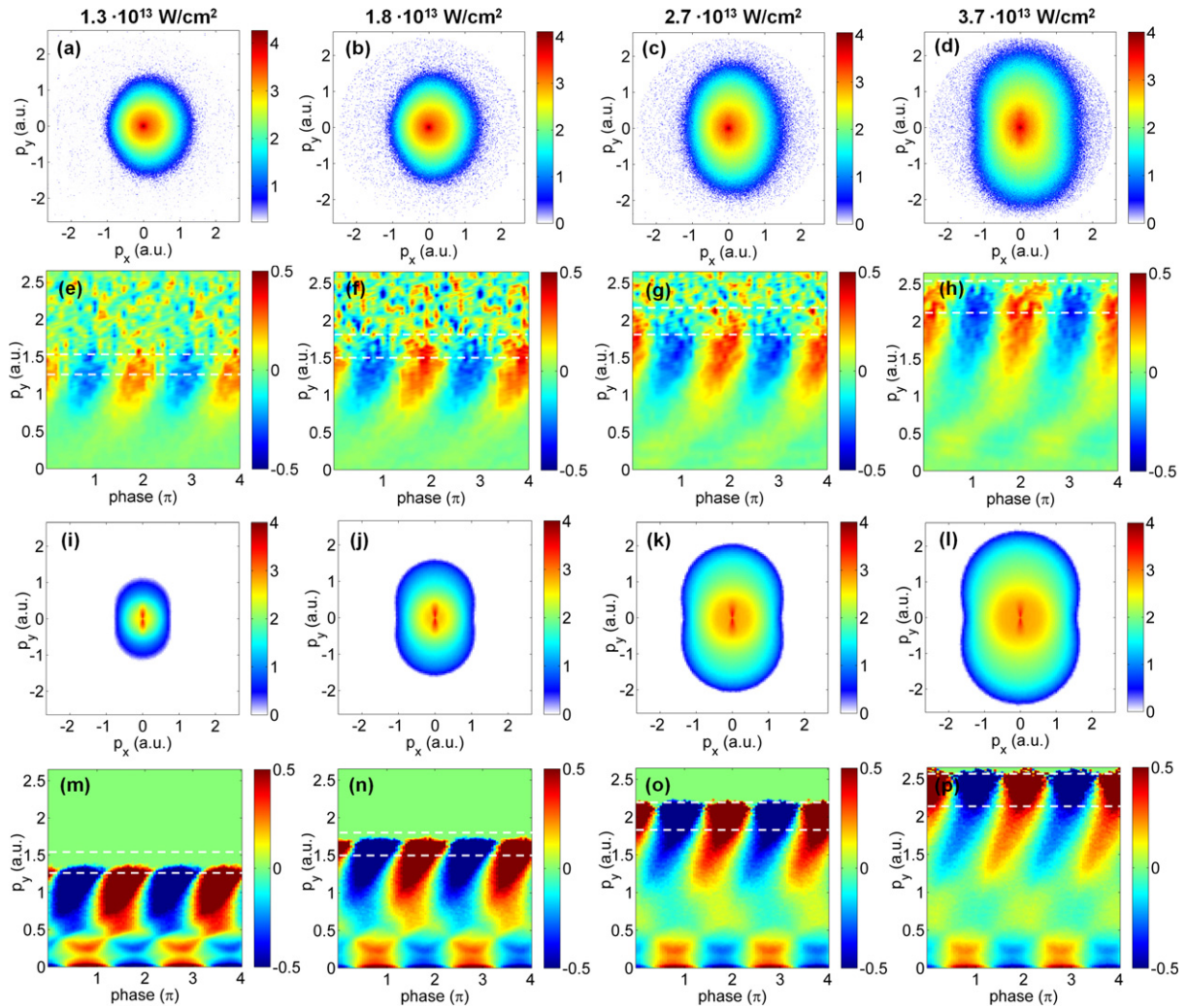


**Figure 3.** Photoelectron emission projection recorded by the VMI averaged over the CEP (log color scale) and asymmetry of the electron emission as a function of the electron momentum and the CEP measured (upper two rows) and calculated (lower two rows) for SiO<sub>2</sub> nanoparticles of 95 nm diameter at different laser intensities, as indicated. The asymmetry maps were obtained by angular integration of the electron yields in the up and down directions within a  $[-45^\circ, +45^\circ]$  range.

calculations performed for the same parameters as in the experiment are also shown in figure 3 (two lower panels).

Two trends can be extracted from the CEP-averaged projections of the momentum distributions. Firstly, all momentum distributions exhibit a similar ellipse-like structure with pronounced cutoffs perpendicular and parallel to the laser polarization axis. The magnitude of the cutoff momentum increases continuously with laser intensity. This behavior is well reproduced by the theory on an absolute scale. Only at lower laser intensity, the measured distributions extend up to slightly larger momenta and are more isotropic as compared to the model calculations. This discrepancy indicates electron emission processes at low laser

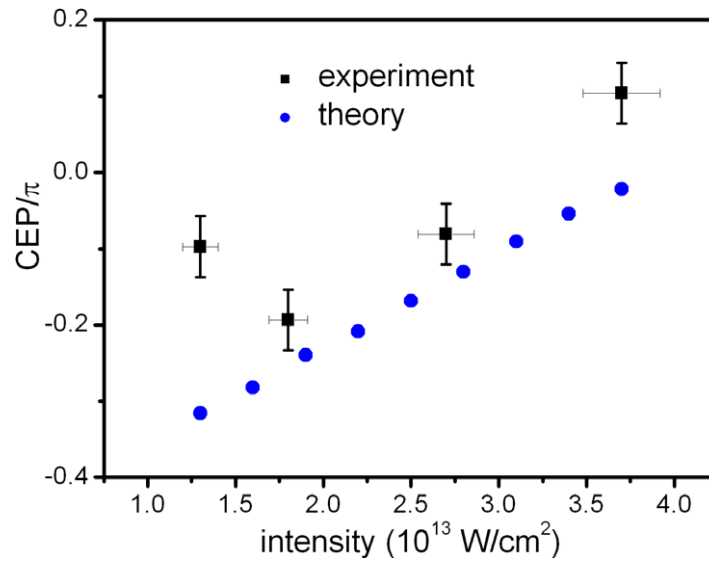


**Figure 4.** CEPs at the maximum asymmetry of the electron emission obtained from the measurements on  $\text{SiO}_2$  nanoparticles of 95 nm diameter at different laser intensities (black boxes) and calculated for the same intensity range (blue filled circles).

intensities (e.g. thermal electron emission) that are not fully accounted for in our model. Secondly, with increasing laser intensity the momentum distributions are more elongated along the laser polarization, i.e. the relative increase of the cutoff momentum along the laser polarization is enhanced. The physical origin of the change in shape is the stronger impact of surface charge effects with increasing intensity. Charge separation after tunnel ionization is enhanced at the poles of the nanoparticle because of the high nonlinearity of the tunnel ionization process. As a result, the relative strength of the corresponding space-charge field at the surface is maximal at the poles when compared to the dielectric near field. As the space-charge field is oriented parallel to the local surface normal, electron acceleration via backscattering is preferentially enhanced along the laser polarization axis. For a more detailed discussion of the effect of the trapping field due to surface space charge, see [8].

In the next step, we focus on the evolution of the phase dependence. Periodic oscillations of the asymmetry parameter with the CEP are present up to the cutoff momentum along the polarization axis for all intensities. The corresponding cutoff energy shows a nearly linear dependence on the laser intensity for the present experimental data with the average value of about  $50U_p$ , in good agreement with our previous studies [8]. The calculated structure of the asymmetry is in good agreement with the measurements. Deviations in the regions of low momenta are mainly attributed to the remaining background gas ATI signal in the measurements and slow, symmetric thermal electron emission from the nanoparticles that are not accounted for in the simulation. Remarkably, the simulation predicts similar intensity-dependent CEP shifts of the asymmetry pattern in the high-energy region. Figure 4 compares measured and calculated CEPs  $\varphi_{\max}$  corresponding to the maximum asymmetry near the cutoff energies for different laser intensities. To obtain these CEP values the asymmetry maps were integrated over  $p_y$  in the cutoff region (in the range of 35–50  $U_p$ , as indicated by the white dashed lines in figure 3) and fitted with a cosine function  $f(\varphi_{\text{CEP}}) = A \cdot \cos(\varphi_{\text{CEP}} - \varphi_{\max})$  for an amplitude  $A$  and phase

$\varphi_{\max}$ . Due to noise, which reduces the asymmetry amplitude near the cutoff in the experiment, the asymmetry amplitudes are not compared. Except for the discrepancy at the lowest laser intensity, theory and experiment indicate a similar increase of  $\varphi_{\max}$  with laser intensity, i.e. a systematic intensity effect in the phase-dependent electron emission beyond the mere increase of the cutoff energy. Since such strong shifts have not been observed on atoms, this behavior is attributed to the additional surface and collective effects in the case of nanoparticles. A closer analysis of the contributions of the different microscopic processes is thus an interesting topic for detailed future studies.

#### 4.2. Imaging the electron rescattering

The angle-resolved electron emission provided by the VMI detection allows for a more detailed analysis of the CEP-dependent part of the electron emission. For each momentum projection on the detector plane,  $(p_x, p_y)$ , the CEP-dependent electron yield was fitted with the function  $A(p_x, p_y, \varphi) = C(p_x, p_y) \times \cos(\varphi + \Delta\varphi(p_x, p_y))$ . From this fit, angular-resolved amplitude,  $C(p_x, p_y)$ , and phase,  $\Delta\varphi(p_x, p_y)$ , maps of the CEP-dependent part of the electron emission were obtained. To increase the signal-to-noise ratio, the image data were binned with a bin size of  $4 \times 4$  pixels (corresponding to an area of  $\sim 0.03 \text{ au} \times 0.03 \text{ au}$  in  $p_y$ - $p_x$  momentum space).

Figure 5 presents the amplitude,  $C(p_x, p_y)$ , and the phase,  $\Delta\varphi(p_x, p_y)$ , maps of the CEP-dependent part of the electron emission (a, b) measured for 95 nm diameter  $\text{SiO}_2$  particles at a laser intensity of  $1.3 \times 10^{13} \text{ W cm}^{-2}$ . The lower panels of figure 5 show the corresponding results of the simulations. The amplitude and the phase distributions extend to the cutoff of the overall electron emission, confirming the contribution of the few-cycle laser-driven electron acceleration to the high-energy electron yield. Comparison with the model calculation shows very good agreement with the measured CEP-dependent electron yield (up to an unknown global scaling factor). The direct electron emission contributes to the signal at low momenta and preferentially along the polarization axis, whereas the rescattering electrons acquire much higher kinetic energies over a broader angular range. The amplitude,  $C(p_x, p_y)$ , exhibits a minimum perpendicular to the laser polarization, and the phase,  $\Delta\varphi(p_x, p_y)$ , experiences a phase jump across the  $p_y = 0$  line.

Measurements at a higher laser intensity of  $3.7 \times 10^{13} \text{ W cm}^{-2}$  show similar CEP-dependent amplitude and phase distributions (figures 6(a) and (b)). A slightly larger extension of the CEP-dependent electron emission along the laser polarization at higher intensity can be attributed to the effect of the mean field of free charges originating from the caps of the nanoparticle.

From the comparison of the measured and calculated momentum-resolved amplitudes and phases of the CEP-dependent signals in figures 5 and 6, two main conclusions can be drawn. Firstly, the amplitude and phase maps exhibit even symmetry along the direction of laser propagation, i.e. with respect to  $p_x = 0$ . This shows that field retardation effects over the size scale of the nanoparticle are negligible and the dipole approximation is valid. A substantial impact of field propagation would lead to (i) higher field enhancement toward the back side of the particle and (ii) a variation of the local CEP on the particle surface. The absence of corresponding distortions in the measured momentum and phase maps demonstrates that both processes do not contribute in the current size regime. Secondly, the amplitude maps show a CEP-dependent signal up to the cutoff, separated circular features for positive and negative values of  $p_y$ , and a clear elongation of the distribution along the laser polarization axis. The presence of the two separate circular features supports that electron backscattering on the surface

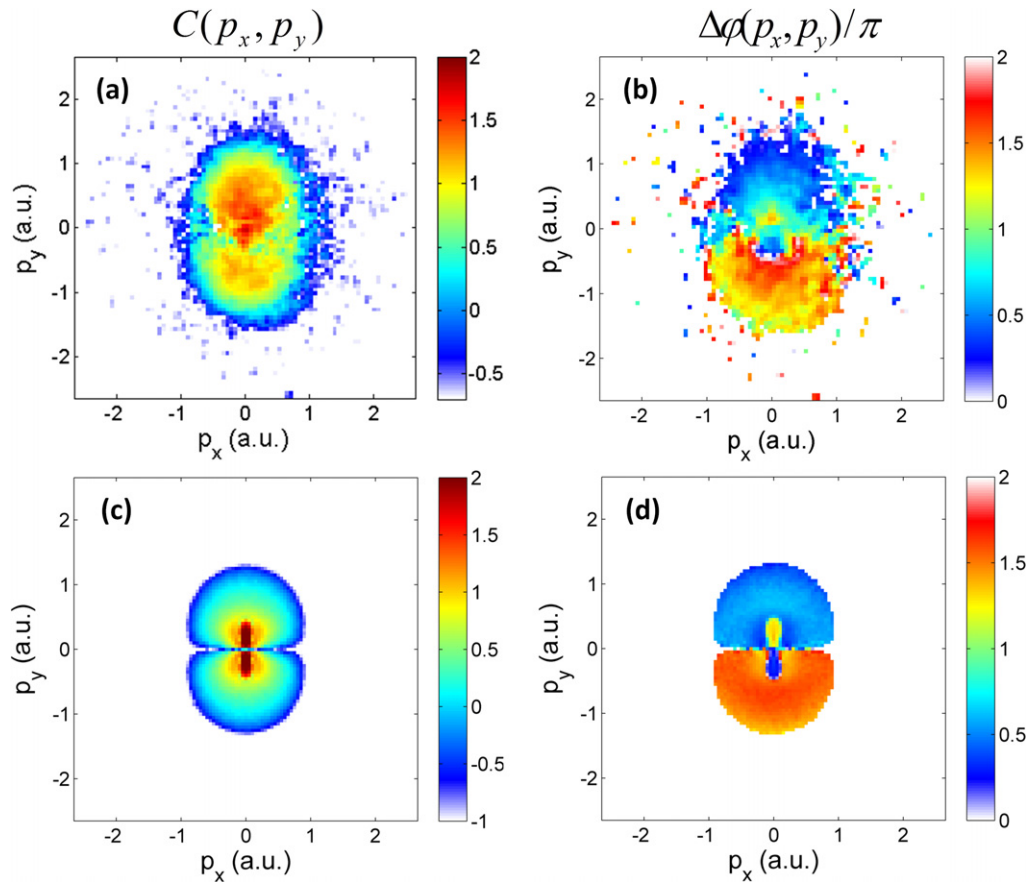


**Figure 5.** Amplitude (a) and phase (b) of the CEP-dependent part of the electron emission obtained from the measurements of SiO<sub>2</sub> nanoparticles of 95 nm diameter for a laser intensity of  $1.3 \times 10^{13} \text{ W cm}^{-2}$ . Amplitude (c) and phase (d) of the CEP-dependent part of the electron emission calculated for SiO<sub>2</sub> nanoparticles of 95 nm diameter at a laser intensity of  $1.3 \times 10^{13} \text{ W cm}^{-2}$ .

is a major process behind the CEP-dependent electron acceleration, as discussed in more detail below. Further, the phase maps exhibit an odd symmetry with respect to  $p_y = 0$  containing a sharp phase jump of  $180^\circ$ . This reflects that the effective CEP is flipped by  $180^\circ$  on the upper and lower surfaces of the nanoparticle, underlining the local phase selectivity of the emission from the two sides of the nanoparticle.

In the following, we substantiate the above assignment of the CEP-dependent high-energy electron emission to surface backscattering by a theoretical analysis of partial emission spectra that allows for the identification of the different relevant acceleration processes. To this end, electron spectra are determined from three classes of trajectories distinguished by the number of scattering events. Firstly, trajectories without scattering events correspond to direct emission, i.e. to electrons that do not return to the nanoparticle after their release via tunnel ionization. Direct electrons are driven solely by the laser and the near field in the vicinity of the particle. Secondly, electrons returning to the particle surface for a short period of time undergoing surface backscattering and propagate predominantly in the near field outside of the nanoparticle. This contribution corresponds to trajectories with a low number of scattering events (we chose up to

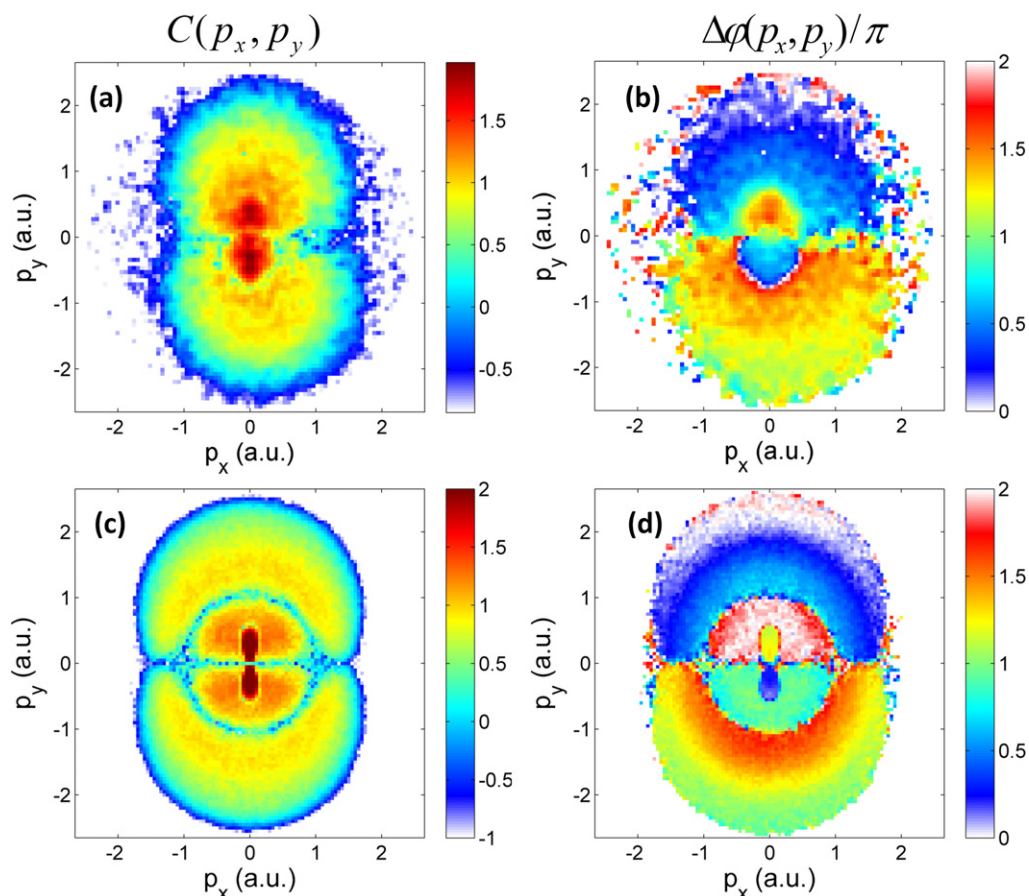


**Figure 6.** Amplitude (a) and phase (b) of the CEP-dependent part of the electron emission obtained from the measurements of SiO<sub>2</sub> nanoparticles of 95 nm diameter for a laser intensity of  $3.7 \times 10^{13} \text{ W cm}^{-2}$ . Amplitude (c) and phase (d) of the CEP-dependent part of the electron emission calculated for SiO<sub>2</sub> nanoparticles of 95 nm diameter at a laser intensity of  $3.7 \times 10^{13} \text{ W cm}^{-2}$ .

five). Thirdly, electrons that reside inside the nanoparticle for a large fraction of the laser pulse undergo collisional heating and can be identified as trajectories with many scattering events (more than five).

The corresponding data for the higher intensity (cf figure 6) are presented in figure 7 and show focus- and CEP-averaged energy spectra (panel (a)) and corresponding projected momentum distributions as determined from the three different classes of trajectories (panels (b)–(d)). Firstly, the contribution of direct emission is negligible in the energy and momentum spectra, reflecting the effect of the trapping potential produced by the surface space charge. The direct electron signal contributes only for low energies and stems from regions with low laser intensities, which contribute to the experimental data due to the focus averaging. At low intensities space-charge trapping is not sufficient to fully suppress the direct emission channel. The backscattering electrons (1–5 collisions) dominate the electron emission (except for very low energies). They exhibit the typical plateau-like structure in the energy spectrum, show a rather sharp cutoff and result in the characteristic, elongated, non-circular feature in the

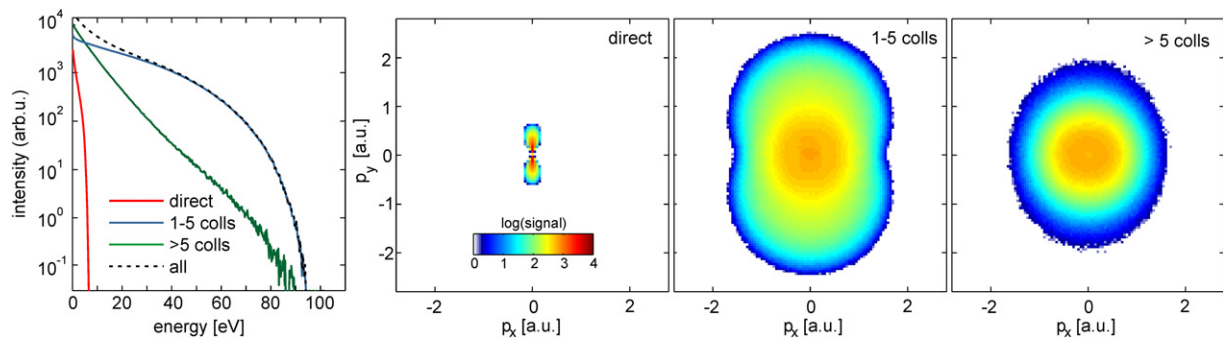


**Figure 7.** Acceleration-processes-resolved electron energy spectra (a) and projected momentum distributions for 95 nm SiO<sub>2</sub> particles at an intensity of  $3.7 \times 10^{13} \text{ W cm}^{-2}$  (focus- and CEP-averaged) as calculated with the mean-field Monte-Carlo model. Contributions from direct, backscattered and collisionally heated electrons are determined by exclusively evaluating trajectories without scattering, with up to five scattering events and more than five scattering events, respectively (as indicated).

projected momentum distribution. The contribution from collisionally heated electrons has a nearly exponential shape in the energy spectrum and produces an almost isotropic feature in the projected momentum distribution. The dominance of backscattering in the high-energy region of the calculated signals indicates that backscattering is the main process for the observed CEP-dependent high-energy electron emission from nanoparticles. This is further supported by the similarity of the corresponding structure in the calculated projected momentum map with the amplitude distribution of the CEP-dependent data in the measurement (figures 5 and 6).

Compared to atomic ATI, the backscattered electrons from nanoparticles show a wider angular distribution. Two effects are responsible for the additional spread. Firstly, in surface regions far away from the nanoparticle poles, the polarization field contains substantial field components perpendicular to the laser polarization. Locally, the emission of most of the energetic backscattered electrons is tilted toward the surface normal. Secondly, the presence of the attractive space-charge field in the surface region increases the relative electron energy gain prior to the moment of recollision [8]. As a result, the angular broadening due to directional redistribution of electron momentum during collision at the surface is increased. The combined action of both mechanisms leads to a significantly wider angular distribution of backscattered electrons as compared to the case of isolated atoms.

## 5. Conclusions and outlook

The phase-controlled high-kinetic-energy electron emission from isolated SiO<sub>2</sub> nanoparticles in strong few-cycle laser fields was investigated in unprecedented detail. Single-shot VMI detection in combination with phase tagging allowed for extended CEP-sensitive measurements with the low-density nanoparticle beam. The main advances achieved in the present study are the determination of the absolute CEP, highly efficient subtraction of spurious background signal and the direct analysis of projected momentum distributions with theory. The observed cutoff energy of the electron emission shows a linear dependence on the laser intensity within the range  $(1-4) \times 10^{13} \text{ W cm}^{-2}$  with an average cutoff value of  $\sim 50U_p$ , in good agreement with our

previous findings [8]. The extended analysis of the phase-tagged electron emission data allowed for a separation of the CEP-dependent electron yields originating from the few-cycle-driven electron dynamics from other processes. The comparison of the measured CEP-dependent electron yields with the results of quasi-classical model calculations shows very good agreement and indicates that the energetic electron emission results from rescattering of previously ionized electrons in the dielectrically enhanced near field of the nanoparticle surface and the trapping potential produced by residual ions and other free electrons in the surface region. The symmetry properties of the amplitude and phase maps from the CEP-dependent electron momentum distribution corroborate the dominance of surface backscattering over collisional heating and underline the absence of field propagation effects in the 100 nm size regime of the dielectric nanoparticles.

An extension of the present experiments toward higher laser intensities holds the promise of becoming a fruitful approach to investigating the onset of highly nonlinear processes of the dielectric medium, such as field-induced metallization [11, 49] or optical breakdown. Free nanoparticles would be particularly advantageous for exploring the nonlinear regime, as they provide constantly fresh samples for each laser shot. The CEP-dependent analysis used in our studies on the isolated 95 nm diameter nanospheres can be further applied to larger nanosystems, where the emission is expected to become asymmetric due to nanofocusing effects. Such experiments may elucidate the role of field propagation effects including nonlinear nanofocusing and local field distortions in electron emission and acceleration.

## Acknowledgments

We acknowledge experimental support from Johannes Stierle and Christoph Skrobol. We are grateful to W Siu and K Schafer for making their TDSE calculations available to us. Financial support from the Chemical Sciences, Geosciences, and Biosciences Division, Office of Basic Energy Sciences, Office of Science, US Department of Energy, the National Science Foundation under CHE-0822646 and EPS-0903806, the EU via the training network ATTOFEL and LaserLab Europe, the DFG via the Emmy-Noether program, SPP1391, grants PA 730/4, SFB652/2 and the Cluster of Excellence: Munich Center for Advanced Photonics (MAP), is gratefully acknowledged. Computer time has been provided by the North-German Supercomputing Alliance (HLRN) within grant no. MVP00004. We are also grateful for support from the King-Saud University in the framework of the MPQ-KSU collaboration and the Visiting Professor program. We acknowledge fruitful collaboration with GSVitec GmbH for improving the image acquisition software.

## References

- [1] Krausz F and Ivanov M 2009 *Rev. Mod. Phys.* **81** 163–234
- [2] Kling M F and Vrakking M J J 2008 *Annu. Rev. Phys. Chem.* **59** 463–92
- [3] Paulus G G, Lindner F, Walther H, Baltuška A, Goulielmakis E, Lezius M and Krausz F 2003 *Phys. Rev. Lett.* **91** 253004
- [4] Bergues B *et al* 2012 *Nature Commun.* **3** 803
- [5] Baltuska A *et al* 2003 *Nature* **421** 611–5
- [6] Kling M F *et al* 2006 *Science* **312** 246
- [7] Znakovskaya I, von den Hoff P, Zherebtsov S, Wirth A, Herrwerth O, Vrakking M J J, de Vivie-Riedle R and Kling M F 2009 *Phys. Rev. Lett.* **103** 103002

- [8] Zherebtsov S *et al* 2011 *Nature Phys.* **7** 656
- [9] Krüger M, Schenk M and Hommelhoff P 2011 *Nature* **475** 78–81
- [10] Apolonski A *et al* 2004 *Phys. Rev. Lett.* **92** 073902
- [11] Durach M, Rusina A, Kling M F and Stockman M I 2011 *Phys. Rev. Lett.* **107** 086602
- [12] Dombi P, Rác P and Bódi B 2009 *Laser Part. Beams* **27** 291–6
- [13] Stebbings S L, Süßmann F, Yang Y-Y, Scrinzi A, Durach M, Rusina A, Stockman M I and Kling M F 2011 *New J. Phys.* **13** 073010
- [14] Zawadzka J, Jaroszynski D A, Carey J J and Wynne K 2001 *Appl. Phys. Lett.* **79** 2130–2
- [15] Dombi P *et al* 2010 *Opt. Exp.* **18** 24206–12
- [16] Kim S, Jin J, Kim Y J, Park I-Y, Kim Y and Kim S-W 2008 *Nature* **453** 757
- [17] Park I-Y, Kim S, Choi J, Kling M F, Stockman M I and Kim S-W 2011 *Nature Photonics* **5** 677
- [18] Goulielmakis E, Yakovlev V S, Cavalieri A L, Uiberacker M, Pervak V, Apolonski A, Kienberger R, Kleineberg U and Krausz F 2007 *Science* **317** 769
- [19] Abel M, Neumark D M, Leone S R and Pfeifer T 2011 *Laser Photonics Rev.* **5** 352
- [20] Udem T, Holzwarth R and Hänsch T W 2002 *Nature* **416** 233–7
- [21] Wittmann T, Horvath B, Helml W, Schätzel M G, Gu X, Cavalieri A L, Paulus G G and Kienberger R 2009 *Nature Phys.* **5** 357–62
- [22] Süßmann F *et al* 2011 *Rev. Sci. Instrum.* **82** 093109
- [23] Johnson N G *et al* 2011 *Phys. Rev. A* **83** 013412
- [24] Ahmad I, Bergé L, Major Z, Krausz F, Karsch S and Trushin S A 2011 *New J. Phys.* **13** 093005
- [25] Ahmad I *et al* 2009 *Appl. Phys. B* **97** 529
- [26] Stöber W, Fink A and Bohn E 1968 *J. Colloid Interface Sci.* **26** 62–9
- [27] Philipse A P 1988 *Colloid Polym. Sci.* **266** 1174–80
- [28] Bogush G H and Zukoski Iv C F 1991 *J. Colloid Interface Sci.* **142** 19–34
- [29] Van Blaaderen A, Van Geest J and Vrij A 1992 *J. Colloid Interface Sci.* **154** 481–501
- [30] Shu J, Wilson K R, Ahmed M, Leone S R, Graf C and Rühl E 2006 *J. Chem. Phys.* **124** 034707–9
- [31] Bresch H, Wassermann B, Langer B, Graf C, Flesch R, Becker U, Osterreicher B, Leisner T and Rühl E 2008 *Faraday Disc.* **137** 389–402
- [32] Wang X and McMurry P H 2006 *Aerosol Sci. Technol.* **40** 320
- [33] Micheau S, Chen Z, Le A T, Rauschenberger J, Kling M F and Lin C D 2009 *Phys. Rev. Lett.* **102** 073001
- [34] Busuladžić M, Gazibegović-Busuladžić A and Milošević D 2006 *Laser Phys.* **16** 289–93
- [35] Sayler A M, Rathje T, Müller W, Rühle K, Kienberger R and Paulus G G 2011 *Opt. Lett.* **36** 1–3
- [36] Kling M F, Rauschenberger J, Verhoef A J, Hasovic E, Uphues T, Milosevic D B, Muller H G and Vrakking M J J 2008 *New J. Phys.* **10** 025024
- [37] Jacoboni C and Reggiani L 1983 *Rev. Mod. Phys.* **55** 645
- [38] Khlebtsov B N, Khanadeev V A and Khlebtsov N G 2008 *Langmuir* **24** 8964–70
- [39] Jackson J 1998 *Classical Electrodynamics* 3rd edn (New York: Wiley)
- [40] Otake T, Yabana K and Iwata J I 2009 *J. Phys.: Condens. Mater* **21** 064224
- [41] Audebert P *et al* 1994 *Phys. Rev. Lett.* **73** 1990
- [42] Temnov V V, Sokolowski-Tinten K, Zhou P, El-Khamhawy A and von der Linde D 2006 *Phys. Rev. Lett.* **97** 237403
- [43] Paulus G G, Becker W, Nicklich W and Walther H 1994 *J. Phys. B: At. Mol. Opt. Phys.* **27** L703–8
- [44] Paulus G G, Nicklich W, Xu H, Lambropoulos P and Walther H 1994 *Phys. Rev. Lett.* **72** 2851
- [45] Ammosov M V, Delone N B and Krainov V P 1986 *Sov. Phys.—JETP* **64** 1191–4
- [46] Martin W C and Zalubas R 1983 *J. Phys. Chem. Ref. Data* **12** 323–80
- [47] Suzuki M, Ando H, Higashi Y, Takenaka H, Shimada H, Matsubayashi N, Imamura M, Kurosawa S, Tanuma S and Powell C J 2000 *Surf. Interface Anal.* **29** 330–5
- [48] Kuhr J C and Fitting H J 1999 *J. Electron Spectrosc. Relat. Phenom.* **105** 257–73
- [49] Durach M, Rusina A, Kling M F and Stockman M I 2010 *Phys. Rev. Lett.* **105** 053001